

Spin-Blockade Spectroscopy of Si/SiGe Quantum Dots

A. M. Jones, E. J. Pritchett, E. H. Chen, T. E. Keating, R. W. Andrews, J. Z. Blumoff, L. A. De Lorenzo, K. Eng, S. D. Ha, A. A. Kiselev, S. M. Meenehan, S. T. Merkel, J. A. Wright, L. F. Edge, R. S. Ross, M. T. Rakher, M. G. Borselli, A. Hunter
HRL Laboratories, LLC, 3011 Malibu Canyon Road, Malibu, California 90265, USA

We implement a technique for measuring the singlet-triplet energy splitting responsible for spin-to-charge conversion in semiconductor quantum dots. This method, which requires fast, single-shot charge measurement, reliably extracts an energy in the limits of both large and small splittings. We perform this technique on an undoped, accumulation-mode Si/SiGe triple-quantum dot and find that the measured splitting varies smoothly as a function of confinement gate biases. Not only does this demonstration prove the value of having an *in situ* excited-state measurement technique as part of a standard tune-up procedure, it also suggests that in typical Si/SiGe quantum dot devices, spin-blockade can be limited by lateral orbital excitation energy rather than valley splitting.

Qubits based on electrons confined in silicon quantum dots (QDs) benefit from the advantages inherent to many semiconductor platforms: fast control, small form factors, and established fabrication methods. Moreover, mitigation of a dominant decoherence pathway—interactions with non spin-zero nuclei—is possible with isotopic enhancement [1]. These advantages have led to key demonstrations, including extended coherence [2–4] as well as fast, accurate control via a number of techniques including tunnel barrier modulation [5, 6], electron spin resonance [7–9], and induced spin-orbit coupling [10]. Recently, one-qubit randomized benchmarking [7, 11, 12], two-qubit randomized benchmarking [13], and two-qubit entangling sequences [11, 14, 15] have been demonstrated with Si-based qubits.

Many quantum dot based qubits rely on the conversion of electron spin states, which preserve quantum information by interacting weakly with their electrical environment, to charge states for control and measurement. In exchange-based schemes, distinct spin states of two interacting electrons (spin-singlets and spin-triplets) are converted into distinguishable charge states utilizing the well-established principles of Pauli spin blockade (SB)[16]. The robustness of SB relies on the energy separation between the ground-singlet and ground-triplet levels of two electrons occupying the same dot, denoted here as Δ_{SB} . This energy limits state measurement and preparation fidelities by setting the range over which one can achieve spin-to-charge conversion and the accuracy with which one can initialize a ground state singlet in a system at finite temperature [17].

Establishing what sets Δ_{SB} in Si QDs is crucial for qubit design. While orbital excitation energies are, in principle, easily manipulated by changing confining potentials with gate biases, the maximum attainable Δ_{SB} is conventionally thought to be limited by valley splitting, the energy splitting between the two lowest-lying quantized states originating from conduction band valleys of bulk, tensily strained silicon [18]. Two-electron orbital energies are determined by the strength and symmetry of in-plane confinement [16, 19], whereas valley splittings are determined primarily by the details of out-of-plane

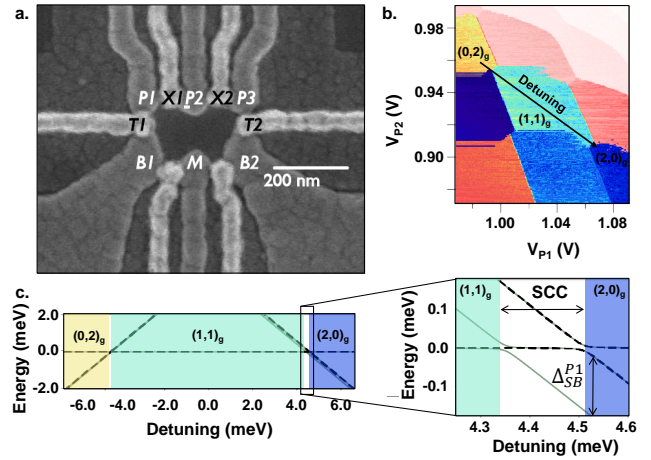


FIG. 1. Device scanning electron micrograph, charge stability, and energy level schematic. **a**, Scanning electron micrograph of a triple-dot device defined by gates P1, P2, P3, with nearby quantum dot electrometer, M. **b**, Charge stability map vs. applied voltage on gates P1 and P2, with color indicating measured current through charge sensor M. **c**, Energy levels vs. detuning of a two-electron Fermi-Hubbard model for spin singlet (solid) and triplet (dashed) states.

electron confinement, a challenge that has inspired many theoretical and engineering efforts [18, 20–22]. Numerous techniques have been used to estimate the magnitude of valley splitting in Si/SiGe quantum dots, including photon-assisted tunneling [23], cavity coupling [24], Landau-Zener-Stückelberg interferometry [25], magneto-transport [22], and magnetospectroscopy [26, 27]. However, the results of these techniques may not accurately measure Δ_{SB} as they probe length scales not generally relevant to QD electrons, require the application of additional electromagnetic fields, or use biasing configurations different from nominal operation. These conditions impede a direct translation of the measured energies to qubit performance.

In this Letter, we describe an excited-state spectroscopy technique which directly measures Δ_{SB} in QDs. The utility of this method lies in its ability to extract

both small and large Δ_{SB} in exactly the bias configuration required to achieve spin-to-charge conversion and without relying on a detailed physical model or the addition of control fields beyond those normally required to operate exchange-only quantum dot qubits. We discuss the requirements placed on our measurement system to perform this technique, which is fundamentally limited by the fidelity of single-shot state discrimination. We then demonstrate this technique on a Si/SiGe double-dot and find Δ_{SB} to be highly tunable and smoothly varying with bias voltages, suggesting that Δ_{SB} in this device is limited by orbital confinement energy rather than valley splitting [28–30]. Both the establishment of a reliable method for *in situ* excited-state spectroscopy and the identification of limitations to device performance should be relevant to many QD architectures.

We measure an accumulation-mode, Si/SiGe triple dot (Fig. 1a) which is similar to other devices [31–35] that have demonstrated both a scalable platform for trapping many electrons [36] and universal qubit control [3, 5]. Building on our previous experience [32, 37], electrons are confined in a tensile-strained Si quantum well, embedded in a strain-relaxed, undoped SiGe alloy. Lateral confinement is provided by two types of overlapping metal gates: large field gates that prevent the accumulation of electrons in undesirable locations and smaller control gates. Quantum dots are defined under the “plunger” gates labeled P_1 , P_2 , and P_3 and are loaded from electron reservoirs under the “bath” gates B_1 and B_2 . Tunneling from the baths to the dots is mediated by the “tunnel” gates T_1 and T_2 , and interdot tunnel coupling is controlled by the “exchange” gates X_1 and X_2 . Bound electrons capacitively couple to the “measure” dot M , with each charge configuration affecting the measured conductance as seen in Fig. 1b. Gate biases provide control of the triple dot through two mechanisms: a linear response in the chemical potentials, which can sensitively calibrate away any residual charge disorder, and an exponential response in tunnel coupling, which allows fast control with large on/off ratios and ultimately facilitates high performance quantum gates.

Spin-to-charge conversion (SCC), by which two-electron spin states are converted into distinct charge states, occurs at biases where two electron number-conserving charge states are nearly degenerate, e.g., bottom-right: (2,0)-(1,1) and top-left: (0,2)-(1,1) of Fig. 1b [16, 38]. As dictated by the Pauli exclusion principle, the two-electron spin-symmetric triplet must be antisymmetric in some other degree of freedom. In silicon, this can be provided by valley, orbital excitation, or some hybridization of the two [28]. The ground-singlet to ground-triplet energy splitting of two electrons occupying dot P_i , denoted $\Delta_{SB}^{P_i}$, determines the range of detunings that support SCC, i.e., biases at which the ground-triplet remains in the (1,1) charge state while the ground-singlet occupies a single QD (see Fig. 1c). These distinct charge states result in different electrostatic potentials at the measure dot, leading to measurably differ-

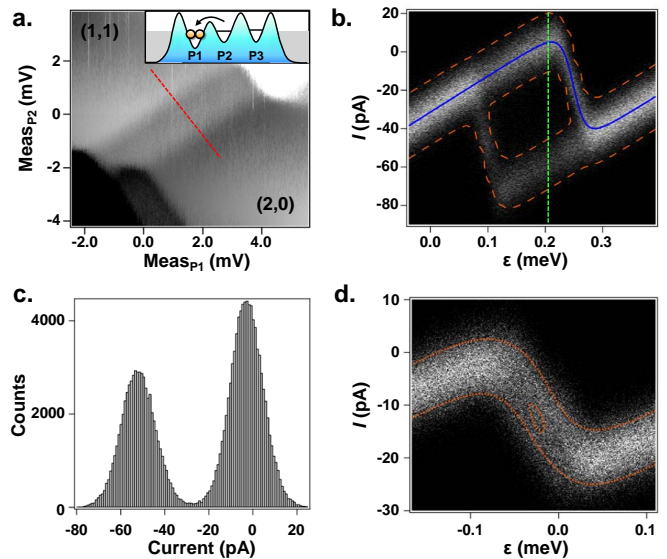


FIG. 2. Single-shot measurements of two-electron ground- and excited-state avoided crossings. **a**, Charge stability scan around the (2,0)-(1,1) avoided crossing, employing a prepare-dephase-measure pulse sequence. Grayscale contrast derives from differential measurement of current through charge sensor M . Inset: Cartoon depicting 1D potential profile of dots P_1 , P_2 , and P_3 for biasing conditions corresponding to the center of the main figure. Moving away from (1,1) towards (2,0) dumps both electrons (yellow circles) into the dot P_1 . **b**, 5000 single-shot measurements taken at each point along the red detuning line in **a**. The vertical axis shows the measured current value, with the horizontal axis giving detuning, in meV, from a point near the (2,0)-(1,1) anticrossing. Grayscale contrast corresponds to the number of counts at each detuning/binning current value. Orange dashed lines show contour line from fit to Eq. (1). Blue line shows the triplet-branch profile from Eq. (3). **c**, 150,000 shot histogram taken at the detuning indicated by the green line in **b**. **d**, data from the (2,0)-(1,1) anticrossing of a second similar device. 500 shots were taken at each detuning. Orange dashed lines show contour line from fit to Eq. (1).

ent conductances at this charge sensor [32].

Our technique measures $\Delta_{SB}^{P_i}$ by analyzing single-shot current values as singlet/triplet mixed states are swept adiabatically through detunings that support spin to charge conversion. This involves a four-step pulse sequence: (1) state preparation, (2) spin dephasing, (3) measurement near SCC, and (4) a final charge reference measurement. In step (1) we prepare a spin-singlet by biasing near the (1,0)-(2,0) charge boundary where fast cotunneling processes quickly relax (2,0) triplets to (2,0) singlets. For step (2), to prepare a mixed state, we adiabatically traverse the (2,0)-(1,1) anticrossing and rapidly pulse to the center of the (1,1) cell. Then the spin-singlet is allowed to dephase in a bath of fluctuating non spin-zero nuclei for 10 μs , which is long compared to the measured $T_2^* \simeq 2 \mu\text{s}$ in this 800 ppm ^{29}Si device. In step (3) the resulting mixed state is rapidly biased back near the (1,1)-(2,0) anticrossing, then adiabatically ramped to

a measurement point, which is swept through detunings near and including SCC. A second measurement (4) is performed deep within the (2,0) cell and subtracted from the first to remove the effects of low-frequency charge noise. This sequence is very similar to those used for standard quantum measurements when operating the device as a singlet-triplet qubit. However, high-fidelity state preparation in step (1) is unnecessary as the remaining steps work identically for a mixture of ground singlets and triplets; therefore this step could be skipped altogether if care is taken that the electrons are not excited out of the singlet/triplet ground state manifold.

The region of SCC is revealed as a step in the contrast of conductance between measurements at steps (2) and (4), apparent in a two-dimensional sweep of the biases on P1 and P2 during the first measurement (see Fig. 2a). We extract the energy Δ_{SB} by taking a line cut (marked in red in Fig. 2a) perpendicular to the region of SCC and repeating the pulse sequence many times at each point along this detuning axis, recording the result of each repetition. This results in a distribution of independently measured currents at each value of detuning. We bin the number of counts at a given detuning within a range of measured current values to obtain the grayscale intensity plot of Fig. 2b, revealing two distinct branches of the transition from the higher-current, (1,1) charge state to the lower-current, (2,0) charge state. With positive detuning defined to be in the (1,1) to (2,0) direction, we ascribe the charge transition that occurs at smaller detuning to a spin singlet state. The transition occurring at larger detuning then corresponds to a spin triplet, separated from the singlet branch by the lowest excited-state energy of both electrons occupying dot P1, $\Delta_{\text{SB}}^{\text{P1}}$. The pulse sequence can easily be modified to sample detunings near the (0,2)-(1,1) anticrossing, with the second charge reference measurement performed deep in the (0,2) charge cell; the resulting data are qualitatively similar to that shown in Fig. 2a, but the extracted energy is $\Delta_{\text{SB}}^{\text{P2}}$. Therefore, with only a slight addition to the pulse sequence, we are able to efficiently measure the excited state energies of two neighboring dots at a given bias configuration. In order to accurately convert the applied detuning bias voltages to an energy scale, we incorporate both the gate lever arm strength and cross-capacitance between dots P_1 and P_2 in calculating a scaling factor. The uncertainty in our measurement of the lever arm constitutes a significant source of uncertainty in our measurement of Δ_{SB} (see Supplemental Section I).

In order to standardize the extraction of Δ_{SB} , we fit the intensity z measured as a function of binned current and detuning (Figure 2b) to the following functional form:

$$z(\Delta_{\text{SB}}) = P_{\text{S}} \cdot f(\epsilon - \epsilon^0, I - (I^0 + m\epsilon), t_c^{\text{S}}) + P_{\text{T}} \cdot f(\epsilon - \epsilon^0 - \Delta_{\text{SB}}, I - (I^0 + m\epsilon), t_c^{\text{T}}) \quad (1)$$

where P_{S} and P_{T} are the relative populations of ground-singlet and ground-triplet with tunnel couplings t_c^{S} and t_c^{T} , respectively. ϵ is the dot-to-dot detuning in units of energy, and ϵ^0 is the detuning energy of the spin-singlet

charge transition. I is the differential current through dot M, with constant offset I^0 and linear offset $m\epsilon$; the slope m stems from a linear cross-capacitance between dots P_1/P_2 and dot M. The function

$$f(\epsilon, I, t_c) = \exp \left[-\frac{1}{2\sigma_I^2} (I - g(\epsilon, t_c))^2 \right] \quad (2)$$

describes the current broadening by an amount σ_I of

$$g(\epsilon, t_c) = I_{\text{amp}} \left[\frac{\epsilon}{\sqrt{\epsilon^2 + 4t_c^2}} \right] \tanh \left[\frac{\sqrt{\epsilon^2 + 4t_c^2}}{2k_{\text{B}}T_e} \right], \quad (3)$$

the functional form expected for charge-based readout of a charge state anticrossing at finite temperature [39]. I_{amp} gives the amplitude of the current contrast, and T_e is the effective electron temperature. State initialization primarily determines the ratio of the fit spin state populations, $P_{\text{S}}/P_{\text{T}}$.

While these formulae provide a concrete fit model, the splitting extracted from this technique is largely independent of model details. The midpoint of each branch indicates the electrons' wave function is in an equal superposition of charge states, i.e., at an anticrossing. As long as this assumption holds, the distance between anticrossings will give Δ_{SB} (with no upper-bound), regardless of higher-lying excited states, charge noise, or other effects that might distort the curves. By contrast, other parameters of Eq. (1), in particular t_c and T_e , are much more sensitive to the precise fit model (see Supplemental Section V). Although these model parameters give insight into the physics responsible for the measured lineshapes, in practice they only capture the slopes of the curves.

In the case of dot P1 where the two branches are well-separated, the energy-referred width of the SCC region in Fig. 2a serves as a reasonably good estimate of Δ_{SB} , up to corrections of order t_c . However, when SCC is not as robust, our technique is still effective at extracting Δ_{SB} . Figure 2d shows data, taken from a similar device, in which the branches are not visibly distinct. Though the horizontal separation between branches only manifests as a widening of the combined curve near the anticrossings, we are still able to extract Δ_{SB} . To bound our confidence in such a fit, we consider the extreme case of trying to determine Δ_{SB} from a single histogram (i.e. a vertical slice of a plot like Fig. 2d). Using Eq. (3) we can relate Δ_{SB} to the separation of the histogram peaks, $\eta \equiv g(\frac{\Delta_{\text{SB}}}{2}, t_c) - g(-\frac{\Delta_{\text{SB}}}{2}, t_c)$. The remaining parameters of Eqs. (1-3) can be fit to high precision, even at low splitting, so finding Δ_{SB} reduces to a problem of fitting the separation between mixed Gaussian distributions with finite statistics.

Given N single-shot measurements, we can calculate a confidence interval comparing an estimated $\tilde{\Delta}_{\text{SB}}$ to the actual Δ_{SB} . This calculation (performed in detail in Sup-

plemental Section IV) gives

$$\begin{aligned} \tilde{\Delta}_{\text{SB}} &\approx \Delta_{\text{SB}} \pm \Delta_{\text{SB}} \frac{\text{erf}^{-1}(C)}{\sqrt{N}} \left[1 + \frac{\sigma_I^2}{\eta^2 P_S P_T} \right], \\ \eta &\approx \frac{I_{\text{amp}}}{2t_c} \tanh\left(\frac{t_c}{k_B T_e}\right) \Delta_{\text{SB}}, \end{aligned} \quad (4)$$

where erf^{-1} is the inverse error function and C is the confidence of the estimate (e.g. $\text{erf}^{-1}(.95) \approx 1.39$ for 95% confidence). This uncertainty stems from shot noise, and exhibits the standard square root statistical improvement with number of shots. The first error term is the standard error in estimating the width of a distribution, while the second represents the added difficulty of measuring a separation between mixed Gaussians that is small compared to their individual variances. Though the splitting ($\Delta_{\text{SB}} = 28.1 \mu\text{eV}$) from the fit shown in Fig. 2d is of the same order as both the tunnel coupling ($t_c = 40.5 \mu\text{eV}$) and thermal broadening ($k_B T_e = 8.6 \mu\text{eV}$), the last term in Eq. (4) gives an uncertainty of $\sim 2.5 \mu\text{eV}$ due to histogram width (with 95% confidence). Note that in practice, we never fit Δ_{SB} to just one histogram; fitting to the full dataset—including an estimate of η at each detuning—adds confidence to our estimate, so this uncertainty is an upper bound. Nonetheless, it shows that our technique can confidently measure splittings in real devices below $30 \mu\text{eV}$, or lower with additional averaging.

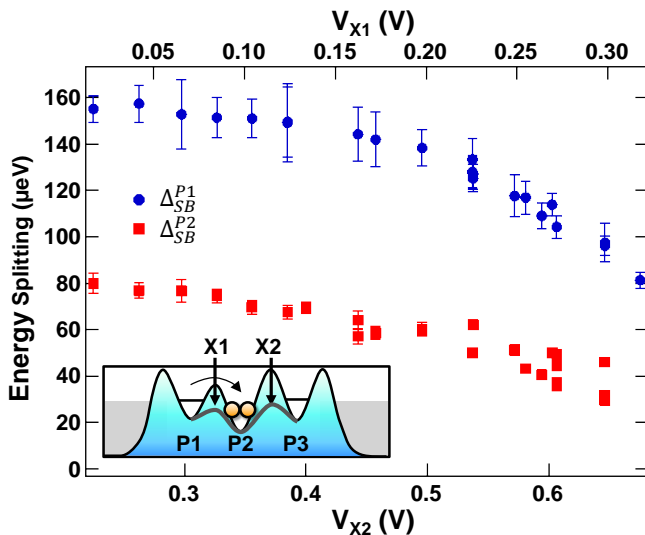


FIG. 3. Exchange gate modulation of two-electron excited-state energy. Measured ground-to-excited state energy separation of dots $P1$ (blue) and $P2$ (red) as a function of voltage applied to neighboring exchange gates. To maintain spin-to-charge conversion, each $X2$ voltage (bottom axis) was compensated with an $X1$ voltage (top axis). Error bars: uncertainty calculated from Eqn. (4) for $C = 0.95$.

For dots with splittings greater than the tunnel coupling, the signal-to-noise ratio (SNR) of the singlet-triplet measurement is not fundamentally limited by t_c or T_e , but rather solely by σ_I and the current discrimination observed between the (1,1) and (2,0) charge states.

Such is the case for dot $P1$, with an SNR of 6.5 near $\epsilon = \Delta_{\text{SB}}/2$ (shown in Fig. 2c). This limit is apparent by noting that at the detuning indicated by the dashed green line of Fig. 2b, the two branches are fully (1,1) and (2,0) in character. The measured current contrast is dictated by the capacitive coupling from dots $P1$ and $P2$ to the charge sensor, a property of this particular gate design. The uncertainty in the measured current, σ_I , of 7.6 pA is accounted for by the contributions of $1/f$ charge noise (3.7 pA broadening for $5 \mu\text{V}/\sqrt{\text{Hz}}$ at 1 Hz of gate-referred noise), Johnson noise (4.3 pA), HEMT input-referred noise (3.7 pA), and shot noise (3.6 pA) as described in Supplemental Section II.

A critical aspect of accurately resolving Δ_{SB} using this technique is our ability to perform single-shot charge measurements at timescales much shorter than singlet-triplet T_1 processes. Since the measurement uncertainty scales quadratically with histogram width, σ_I , the blurring of singlet and triplet histograms caused by T_1 decay during measurement is detrimental, especially when a small Δ_{SB} and/or a high electron temperature limits SNR on fast timescales. Near the region of SCC, we typically observe $T_1 > 100 \mu\text{s}$, while the total measurement integration times of steps (3) and (4) are $12.5 \mu\text{s}$. This fast measurement time is accomplished by mounting cryogenic HEMTs near the device to reduce parasitic capacitance[40], resulting in 60 dB of low-noise amplification up to 1 MHz.

We now use this technique to measure how changes in confining potential affect Δ_{SB} of dots $P1$ and $P2$. We sweep the bias voltages on gates $X1$ and $X2$ at a constant ratio, as indicated by the bottom and top axes of Fig. 3, to deform the confinement potentials while maintaining interdot tunnel couplings amenable to SCC. We observe that the energy splittings for each dot decrease with bias voltage by a factor of ~ 2 , with maximum values of $\sim 150 \mu\text{eV}$ for Δ_{SB}^{P1} and $\sim 80 \mu\text{eV}$ for Δ_{SB}^{P2} . We can rule out a continuous variation of the gate-dot lever arm as the source of this effect (see Supplemental Section I) and conclude that the underlying energy splitting is changing.

Identifying the physics responsible for this variation is challenging but important to improve device performance. The relatively smooth, correlated change in Δ_{SB} over a wide range of biases suggests that valley splitting alone is not responsible: shifting wave functions would sample disorder at the interface of a SiGe alloy in a more random fashion [21, 41]. Also unlikely is an arrangement of steps that would cause valley splittings to change with bias on distinct dots at nearly the same rate[42]. Vertical electric fields easily tune valley splitting in MOS Si quantum dots [17, 30], but the effect is much weaker in Si/SiGe, especially when controlled by neighboring barrier gates. We therefore posit that in this case, the most likely cause of the change in Δ_{SB} with bias is a modification of the two-electron orbital confinement energy, i.e., the wave functions become more elliptical with forward bias on the barrier gates [16, 19]. We note that valley-orbit hybridization is also possible and could be the cause

of an apparent saturation in Δ_{SB} at tighter confinements [28]. Even though we believe that this device is limited by orbital splittings, we expect valley splittings to be similar in magnitude [22]. The delicate interplay between these two degrees of freedom necessitates an *in situ* measurement technique as described here.

In summary, we have described an excited-state spectroscopy method for measuring the two-electron ground-to-excited state energy separation of quantum dots. The measured energy splitting is directly relevant to state

preparation and measurement of singlet/triplet based qubits. This technique, which is only suitable in systems where charge measurements are possible within spin T_1 , is applied to quantum dots tuned for spin-to-charge conversion. In showing the tunability of Δ_{SB} with confinement gate bias, we demonstrate the utility of this technique in optimizing device performance. This measurement technique should be useful to all quantum dot architectures that require robust spin-blockade.

The authors gratefully acknowledge T. Ladd, M. Gyure, M. Reed, A. Pan, D. Kim for helpful discussions.

-
- [1] Thaddeus D. Ladd and Malcolm S. Carroll, “Silicon qubits,” in *Encyclopedia of Modern Optics (Second Edition)*, edited by Bob D. Guenther and Duncan G. Steel (Elsevier, Oxford, 2018) second edition ed., pp. 467–477.
- [2] Juha T. Muhonen, Juan P. Dehollain, Arne Laucht, Fay E. Hudson, Rachpon Kalra, Takeharu Sekiguchi, Kohei M. Itoh, David N. Jamieson, Jeffrey C. McCallum, Andrew S. Dzurak, and Andrea Morello, “Storing quantum information for 30 seconds in a nanoelectronic device,” *Nature Nanotechnology* **9**, 986 (2014).
- [3] Kevin Eng, Thaddeus D. Ladd, Aaron Smith, Matthew G. Borselli, Andrey A. Kiselev, Bryan H. Fong, Kevin S. Holabird, Thomas M. Hazard, Biqin Huang, Peter W. Deelman, Ivan Milosavljevic, Adele E. Schmitz, Richard S. Ross, Mark F. Gyure, and Andrew T. Hunter, “Isotopically enhanced triple-quantum-dot qubit,” *Science Advances* **1** (2015), 10.1126/sciadv.1500214.
- [4] Jun Yoneda, Kenta Takeda, Tomohiro Otsuka, Takashi Nakajima, Matthieu R. Delbecq, Giles Allison, Takumu Honda, Tetsuo Kodera, Shunri Oda, Yusuke Hoshi, Noritaka Usami, Kohei M. Itoh, and Seigo Tarucha, “A quantum-dot spin qubit with coherence limited by charge noise and fidelity higher than 99.9%,” *Nature Nanotechnology* **13**, 102–106 (2018).
- [5] M. D. Reed, B. M. Maune, R. W. Andrews, M. G. Borselli, K. Eng, M. P. Jura, A. A. Kiselev, T. D. Ladd, S. T. Merkel, I. Milosavljevic, E. J. Pritchett, M. T. Rakher, R. S. Ross, A. E. Schmitz, A. Smith, J. A. Wright, M. F. Gyure, and A. T. Hunter, “Reduced sensitivity to charge noise in semiconductor spin qubits via symmetric operation,” *Phys. Rev. Lett.* **116**, 110402 (2016).
- [6] Frederico Martins, Filip K. Malinowski, Peter D. Nissen, Edwin Barnes, Saeed Fallahi, Geoffrey C. Gardner, Michael J. Manfra, Charles M. Marcus, and Ferdinand Kuemmeth, “Noise suppression using symmetric exchange gates in spin qubits,” *Phys. Rev. Lett.* **116**, 116801 (2016).
- [7] M. Veldhorst, J. C. C. Hwang, C. H. Yang, A. W. Leenstra, B. de Ronde, J. P. Dehollain, J. T. Muhonen, F. E. Hudson, K. M. Itoh, A. Morello, and A. S. Dzurak, “An addressable quantum dot qubit with fault-tolerant control-fidelity,” *Nature Nanotechnology* **9**, 981 EP – (2014).
- [8] J T Muhonen, A Laucht, S Simmons, J P Dehollain, R Kalra, F E Hudson, S Freer, K M Itoh, D N Jamieson, J C McCallum, A S Dzurak, and A Morello, “Quantifying the quantum gate fidelity of single-atom spin qubits in silicon by randomized benchmarking,” *Journal of Physics: Condensed Matter* **27**, 154205 (2015).
- [9] M. A. Fogarty, K. W. Chan, B. Hensen, W. Huang, T. Tanttu, C. H. Yang, A. Laucht, M. Veldhorst, F. E. Hudson, K. M. Itoh, D. Culcer, A. Morello, and A. S. Dzurak, “Integrated silicon qubit platform with single-spin addressability, exchange control and robust single-shot singlet-triplet readout,” arXiv:1708.03445 (2017).
- [10] Erika Kawakami, Thibaut Jullien, Pasquale Scarlino, Daniel R. Ward, Donald E. Savage, Max G. Lagally, Viatcheslav V. Dobrovitski, Mark Friesen, Susan N. Coppersmith, Mark A. Eriksson, and Lieven M. K. Vandersypen, “Gate fidelity and coherence of an electron spin in an si/sige quantum dot with micromagnet,” *Proceedings of the National Academy of Sciences* **113**, 11738–11743 (2016), <http://www.pnas.org/content/113/42/11738.full.pdf>.
- [11] D. M. Zajac, A. J. Sigillito, M. Russ, F. Borjans, J. M. Taylor, G. Burkard, and J. R. Petta, “Resonantly driven cnot gate for electron spins,” *Science* (2017), 10.1126/science.aao5965.
- [12] C. H. Yang, K. W. Chan, R. Harper, W. Huang, T. Evans, J. C. C. Hwang, B. Hensen, A. Laucht, T. Tanttu, F. E. Hudson, S. T. Flammia, K. M. Itoh, A. Morello, S. D. Bartlett, and A. S. Dzurak, “Silicon qubit fidelities approaching stochastic noise limits via pulse optimisation,” arXiv:1807.09500 (2018).
- [13] W. Huang, C. H. Yang, K. W. Chan, T. Tanttu, B. Hensen, R. C. C. Leon, M. A. Fogarty, J. C. C. Hwang, F. E. Hudson, K. M. Itoh, A. Morello, A. Laucht, and A. S. Dzurak, “Fidelity benchmarks for two-qubit gates in silicon,” (2018), arXiv:1805.05027.
- [14] M. Veldhorst, C. H. Yang, J. C. C. Hwang, W. Huang, J. P. Dehollain, J. T. Muhonen, S. Simmons, A. Laucht, F. E. Hudson, K. M. Itoh, A. Morello, and A. S. Dzurak, “A two-qubit logic gate in silicon,” *Nature* **526**, 410 (2015).
- [15] T. F. Watson, S. G. J. Philips, E. Kawakami, D. R. Ward, P. Scarlino, M. Veldhorst, D. E. Savage, M. G. Lagally, Mark Friesen, S. N. Coppersmith, M. A. Eriksson, and L. M. K. Vandersypen, “A programmable two-qubit quantum processor in silicon,” *Nature* **555**, 633 (2018).
- [16] R. Hanson, L. P. Kouwenhoven, J. R. Petta, S. Tarucha, and L. M. K. Vandersypen, “Spins in few-electron quantum dots,” *Rev. Mod. Phys.* **79**, 1217–1265 (2007).
- [17] John King Gamble, Patrick Harvey-Collard, N. Tobias

- Jacobson, Andrew D. Baczewski, Erik Nielsen, Leon Maurer, Ins Montao, Martin Rudolph, M. S. Carroll, C. H. Yang, A. Rossi, A. S. Dzurak, and Richard P. Muller, "Valley splitting of single-electron si mos quantum dots," *Applied Physics Letters* **109**, 253101 (2016), <https://doi.org/10.1063/1.4972514>.
- [18] Timothy B. Boykin, Gerhard Klimeck, M. A. Eriksson, Mark Friesen, S. N. Coppersmith, Paul von Allmen, Fabiano Oyafuso, and Seungwon Lee, "Valley splitting in strained silicon quantum wells," *Applied Physics Letters* **84**, 115–117 (2004), <https://doi.org/10.1063/1.1637718>.
- [19] Dmitriy V. Melnikov and Jean-Pierre Leburton, "Dimensionality effects in the two-electron system in circular and elliptic quantum dots," *Phys. Rev. B* **73**, 085320 (2006).
- [20] Kohei Sasaki, Ryuichi Masutomi, Kiyohiko Toyama, Kentarou Sawano, Yasuhiro Shiraki, and Tohru Okamoto, "Well-width dependence of valley splitting in si/sige quantum wells," *Applied Physics Letters* **95**, 222109 (2009), <https://doi.org/10.1063/1.3270539>.
- [21] Lijun Zhang, Jun-Wei Luo, Andre Saraiva, Belita Koiller, and Alex Zunger, "Genetic design of enhanced valley splitting towards a spin qubit in silicon," *Nature Communications* **4**, 2396 (2013), article.
- [22] Samuel F. Neyens, Ryan H. Foote, Brandur Thorgrimson, T. J. Knapp, Thomas McJunkin, L. M. K. Vandersypen, Payam Amin, Nicole K. Thomas, James S. Clarke, D. E. Savage, M. G. Lagally, Mark Friesen, S. N. Coppersmith, and M. A. Eriksson, "The critical role of substrate disorder in valley splitting in si quantum wells," *Applied Physics Letters* **112**, 243107 (2018), <https://doi.org/10.1063/1.5033447>.
- [23] W. G. van der Wiel, S. De Franceschi, J. M. Elzerman, T. Fujisawa, S. Tarucha, and L. P. Kouwenhoven, "Electron transport through double quantum dots," *Rev. Mod. Phys.* **75**, 1–22 (2002).
- [24] X. Mi, Csaba G. Péterfalvi, Guido Burkard, and J. R. Petta, "High-resolution valley spectroscopy of si quantum dots," *Phys. Rev. Lett.* **119**, 176803 (2017).
- [25] Joshua S. Schoenfeld, Blake M. Freeman, and Hong-Wen Jiang, "Coherent manipulation of valley states at multiple charge configurations of a silicon quantum dot device," *Nature Communications* **8**, 64 (2017).
- [26] W H Lim, C H Yang, F A Zwanenburg, and A S Dzurak, "Spin filling of valley-orbit states in a silicon quantum dot," *Nanotechnology* **22**, 335704 (2011).
- [27] M. G. Borselli, K. Eng, E. T. Croke, B. M. Maune, B. Huang, R. S. Ross, A. A. Kiselev, P. W. Deelman, I. Alvarado-Rodriguez, A. E. Schmitz, M. Sokolich, K. S. Holabird, T. M. Hazard, M. F. Gyure, and A. T. Hunter, "Pauli spin blockade in undoped si/sige two-electron double quantum dots," *Applied Physics Letters* **99**, 063109 (2011), <https://doi.org/10.1063/1.3623479>.
- [28] Mark Friesen and S. N. Coppersmith, "Theory of valley-orbit coupling in a si/sige quantum dot," *Phys. Rev. B* **81**, 115324 (2010).
- [29] Zhan Shi, C. B. Simmons, J. R. Prance, John King Gamble, Mark Friesen, D. E. Savage, M. G. Lagally, S. N. Coppersmith, and M. A. Eriksson, "Tunable singlet-triplet splitting in a few-electron si/sige quantum dot," *Applied Physics Letters* **99**, 233108 (2011), <https://doi.org/10.1063/1.3666232>.
- [30] C. H. Yang, A. Rossi, R. Ruskov, N. S. Lai, F. A. Mohiyaddin, S. Lee, C. Tahan, G. Klimeck, A. Morello, and A. S. Dzurak, "Spin-valley lifetimes in a silicon quantum dot with tunable valley splitting," *Nature Communications* **4**, 2069 EP – (2013), article.
- [31] N. S. Lai, W. H. Lim, C. H. Yang, F. A. Zwanenburg, W. A. Coish, F. Qassemi, A. Morello, and A. S. Dzurak, "Pauli spin blockade in a highly tunable silicon double quantum dot," *Scientific Reports* **1**, 110 (2011), article.
- [32] M. G. Borselli, K. Eng, R. S. Ross, T. M. Hazard, K. S. Holabird, B. Huang, A. A. Kiselev, P. W. Deelman, L. D. Warren, I. Milosavljevic, A. E. Schmitz, M. Sokolich, M. F. Gyure, and A. T. Hunter, "Undoped accumulation-mode si/sige quantum dots," *Nanotechnology* **26**, 375202 (2015).
- [33] D. M. Zajac, T. M. Hazard, X. Mi, K. Wang, and J. R. Petta, "A reconfigurable gate architecture for si/sige quantum dots," *Applied Physics Letters* **106**, 223507 (2015), <https://doi.org/10.1063/1.4922249>.
- [34] Daniel R. Ward, Dohun Kim, Donald E. Savage, Max G. Lagally, Ryan H. Foote, Mark Friesen, Susan N. Coppersmith, and Mark A. Eriksson, "State-conditional coherent charge qubit oscillations in a si/sige quadruple quantum dot," *Npj Quantum Information* **2**, 16032 (2016), article.
- [35] S. A. Studenikin, L. Gaudreau, K. Kataoka, D. G. Austing, and A. S. Sachrajda, "Enhancement-mode two-channel triple quantum dot from an undoped si/si_{0.8}ge_{0.2} quantum well hetero-structure," *Applied Physics Letters* **112**, 233101 (2018), <https://doi.org/10.1063/1.5023596>.
- [36] D. M. Zajac, T. M. Hazard, X. Mi, E. Nielsen, and J. R. Petta, "Scalable gate architecture for a one-dimensional array of semiconductor spin qubits," *Phys. Rev. Applied* **6**, 054013 (2016).
- [37] Peter W. Deelman, Lisa F. Edge, and Clayton A. Jackson, "Metamorphic materials for quantum computing," *MRS Bulletin* **41**, 224230 (2016).
- [38] B. E. Kane, "A silicon-based nuclear spin quantum computer," *Nature* **393**, 133 (1998), article.
- [39] L. DiCarlo, H. J. Lynch, A. C. Johnson, L. I. Childress, K. Crockett, C. M. Marcus, M. P. Hanson, and A. C. Gossard, "Differential charge sensing and charge delocalization in a tunable double quantum dot," *Phys. Rev. Lett.* **92**, 226801 (2004).
- [40] I. T. Vink, T. Nooitgedagt, R. N. Schouten, L. M. K. Vandersypen, and W. Wegscheider, "Cryogenic amplifier for fast real-time detection of single-electron tunneling," *Applied Physics Letters* **91**, 123512 (2007).
- [41] J. C. Abadillo-Uriel, B. Thorgrimsson, D. Kim, L. W. Smith, C. B. Simmons, D.R. Ward, R.H. Foote, J. Corrigan, D. E. Savage, M. G. Lagally, M. J. Caldern, S. N. Coppersmith, M. A. Eriksson, and M. Friesen, "Signatures of atomic-scale structure in the energy dispersion and coherence of a si quantum-dot qubit," (2018), [arXiv:1805.10398](https://arxiv.org/abs/1805.10398).
- [42] Mark Friesen, Sucismita Chutia, Charles Tahan, and S. N. Coppersmith, "Valley splitting theory of SiGeSiSiGe quantum wells," *Phys. Rev. B* **75**, 115318 (2007).

Supplemental Material: Spin-Blockade Spectroscopy of Si/SiGe
Quantum Dots

arXiv:1809.08320v1 [quant-ph] 21 Sep 2018

I. LEVER ARM STRENGTH

Crucial to the accurate extraction of the ground-to-excited state splitting, Δ_{SB} , using the technique described in the main text, is the conversion of detuning from the swept bias voltage to the actual difference in the chemical potential energies of the respective dots. While several methods for doing this have been presented elsewhere (cf. photon assisted tunneling[1, 2]), we outline our two-step process here.

First, we obtain the lever arm strength, α , of each plunger gate by fitting a charge transition width as a function of refrigerator temperature. For the $P1$ plunger gate we monitor the (1,0)-(2,0) charge transition. For the $P2$ plunger gate we monitor the (3,0)-(3,1) charge transition. The measured linewidth of each transition as a function of refrigerator base temperature is shown in Fig. S1. These curves are fit to a phenomenological expression which assumes that contributions to the linewidth stem from an incoherent sum of the measured temperature of the mixing chamber, T_{MC} , and a constant electronic ‘effective’ temperature, T_e , as

$$\Delta V(T_{\text{MC}}) = \frac{k_B \sqrt{T_{\text{MC}}^2 + T_e^2}}{\alpha}. \quad (1)$$

Fits to the data (blue and green lines in Fig. S1) yield $\alpha_{P1} = 0.095$ eV/V and $\alpha_{P2} = 0.104$ eV/V. The difference between α_{P1} and α_{P2} (9%) is much lower than the fitting error and better reflects the variation found within an ensemble of lever arm measurements. The resulting uncertainty in the ratio of detuning biases to energy directly affects the accuracy with which we can extract Δ_{SB} .

Second, we measure the cross capacitance of gate $P2$ on an electron loaded under $P1$ compared to the capacitance of gate $P1$ on the same electron, which we denote $G_{P1,P2}$, by measuring the slope of a $P1$ loading line with respect to bias V_{P2} . $G_{P2,P1}$ can be measured similarly. The four measured factors α_{P1} , α_{P2} , $G_{P1,P2}$, and $G_{P2,P1}$, together with the relative bias swept on gates $P2$ and $P1$ ($\Delta V_{P2}/\Delta V_{P1}$ where $\Delta V_{P1} - \Delta V_{P2}$ is the detuning bias), allow us to convert the $P1$ voltage range supporting spin-blockade, ΔV_{SB} , to energy:

$$\Delta_{\text{SB}} = \left| \alpha_{P1} - \alpha_{P2} \cdot G_{P2,P1} - \frac{\Delta V_{P2}}{\Delta V_{P1}} (\alpha_{P2} - \alpha_{P1} \cdot G_{P1,P2}) \right| \Delta V_{\text{SB}}. \quad (2)$$

One effect which may give rise to the variation in Δ_{SB} with bias discussed in the main text is a varying voltage-to-energy scaling caused by changes in cross capacitance or lever arm strength, α . We account for changes in cross capacitance by updating the values of $G_{P1,P2}$

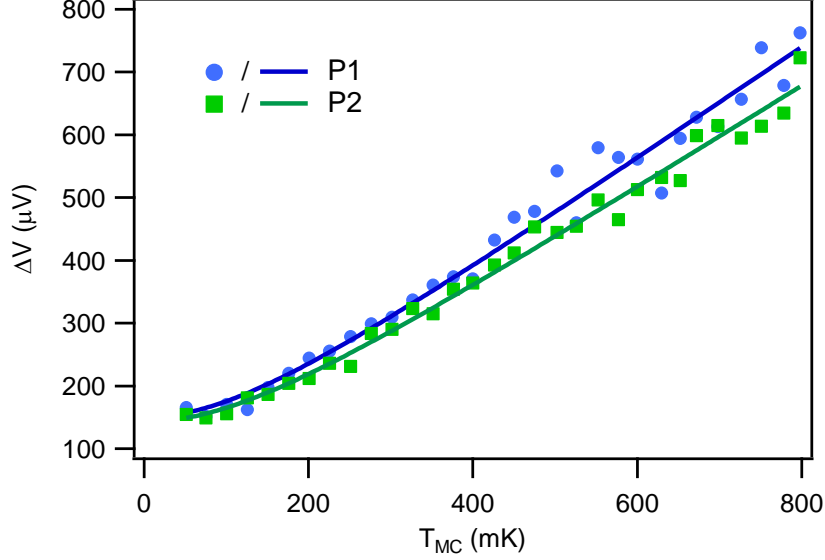


FIG. S1. Charge transition width vs. refrigerator base temperature. Measured width, $\Delta V(T_{MC})$, of the $P1$ (1,0)-(2,0) (blue circles) and $P2$ (3,0)-(3,1) (green squares) charge transitions as a function of refrigerator base temperature, T_{MC} . Blue and green lines show fits to corresponding data sets to extract lever arm strength.

and $G_{P2,P1}$ over the course of the sweep in Fig. 3 of the main text. Although changes in the electrostatic potential can certainly affect α if the electron is localized far from under the center of the corresponding gate, we find this interpretation of the data of main text Figure 3 to be inconsistent with our observations. Measurements of α from devices similar to the one studied here are typically performed in a low-exchange gate biasing regime (e.g. near the left-hand side of Fig. 3). By comparison, the measurements shown here were performed with the $X1$ and $X2$ exchange gates forward biased ($V_{X2} = 0.675$ V and $V_{X1} = 0.318$ V, right-hand side of Fig. 3). The agreement between typical values of lever arm strength (~ 0.1 eV/V) with those measured here contrasts with the factor of two change in Δ_{SB} observed in the main text. Therefore, we conclude that the large tunability of Δ_{SB} is not confounded by significant changes in lever arm strength.

II. CRYOGENIC READOUT ELECTRONICS

Measuring capacitive shifts at the charge sensor requires a chain of cryogenic and room temperature electronics leading to both the source and drain electrodes. Changes in charge

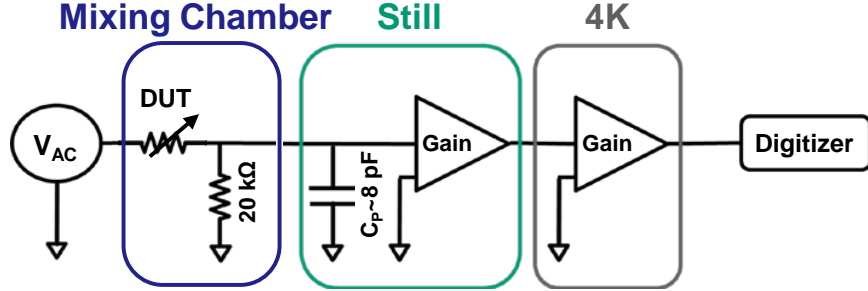


FIG. S2. Experiment measurement chain. At the output of the device under test (DUT), a 20 kOhm shunt resistor on the mixing chamber stage converts current to voltage. With ~ 8 pF of parasitic capacitance, this arrives at the first HEMT amplification stage held at ~ 1 K before passing through the second stage held at ~ 4 K, providing a gain of 60 dB up to 1 MHz.

sensor current are detected using lock-in amplification techniques. The lock-in tone is a series of alternating square pulses from an arbitrary waveform generator at room temperature sent down the source line. This line has 10,000:1 voltage division at room temperature to mitigate voltage noise and is filtered by a commercial low pass filter with a 120 MHz cutoff frequency. Alternating current driven through the charge sensor is converted back into voltage using a ~ 20 kOhm shunt resistor, which reduces the impedance of the high impedance charge sensor (~ 100 kOhm). Since the measured voltage scales linearly with the value of the shunt resistor, we increase our bandwidth by minimizing parasitic capacitance between the drain and the amplifiers, rather than by lowering the resistance. By mounting the pHEMTs on standoffs located near the device [3], we achieve a capacitance of ~ 8 pF, allowing for a measurement bandwidth of 1 MHz, well above the $1/f$ corner frequency of our electronics. The voltage signal is amplified ~ 60 dB using 2 stages of amplification (Avago ATF-38143 pHEMTs) held at ~ 1 K and ~ 4 K. The amplified voltage is delivered using rf coaxial cables and digitized at room temperature using commercial ADCs where the lock-in tone through the charge sensor is demodulated and converted into units of conductance. Components of this measurement chain that contribute to the total noise floor of the measurement include the Johnson noise of the shunt resistor ($332 \text{ pV}/\sqrt{\text{Hz}}$ at 100 mK), shot noise ($253 \text{ pV}/\sqrt{\text{Hz}}$), and the input-referred noise of the pHEMT amplifiers ($\sim 250 \text{ pV}/\sqrt{\text{Hz}}$). Integrating these sources with our measurement filter function and adding the result to the $1/f$ charge noise contribution (3.65 pA broadening for $5 \text{ } \mu\text{V}/\sqrt{\text{Hz}}$ at 1 Hz of gate-referred noise), we obtain

a total broadening of 7.7 pA, in excellent agreement with the observed value of 7.6 pA from Fig. 2c of the main text.

III. FERMI-HUBBARD MODEL FITTING

We derive our fit model, Eqs. (1–3) in the main text, from a Fermi-Hubbard model, following [4]. Near the charge boundaries that support spin-to-charge conversion (SCC), the system’s ground state is a superposition of (1,1) and (2,0) charge states, connected by a two-electron tunnel coupling, t_c , with detuning ϵ . We assume that the electrons have a valley/orbital degree of freedom with excitation energy Δ_{SB} , so that the ground $|g\rangle_{20}$ and excited $|e\rangle_{20}$ states of two-electrons occupying the same dot (the (2,0) charge configuration indicated by subscript) have splitting Δ_{SB} . At detunings near the region of SCC, the system’s ground state is dominated by the lowest allowed energy states: $|g\rangle_{11}$ and $|g\rangle_{02}$ for spin-singlets and $|g\rangle_{11}$ and $|e\rangle_{02}$ for the spin-triplet. $|g\rangle_{02}$ is forbidden for spin-triplets by the Pauli exclusion principle. In this reduced basis, we can write the Hamiltonian as $H = H_S + H_T$ where

$$H_S \approx t_c^S (|g\rangle_{11\ 20} \langle g| + \text{h.c.}) - \epsilon |g\rangle_{20\ 20} \langle g|, \quad (3)$$

$$H_T \approx t_c^T (|g\rangle_{11\ 20} \langle e| + \text{h.c.}) - (\epsilon - \Delta_{\text{SB}}) |e\rangle_{20\ 20} \langle e|, \quad (4)$$

and the singlet and triplet t_c may in principle be different, especially when the excited state is determined by the valley degree of freedom. In this case, t_c^T/t_c^S is a function of the “valley mixing angle”, the rotation from one dot to the other of the relative phase between superpositions of the valley states [5, 6]. The Hamiltonians of Eqs. (3–4) are identical up to an offset in ϵ and potentially different tunnel couplings, so without loss of generality we focus on H_S in the following analysis.

For a given ϵ , H_S has an energy gap of $E(\epsilon, t_c) = \sqrt{\epsilon^2 + 4t_c^2}$, and its ground state has (2,0) population $P_{20} = (1 + \epsilon/E(\epsilon, t_c))/2$. At finite temperature T_e , we will find the system in its excited state with probability $\exp(-E(\epsilon, t_c)/k_B T_e)$. Weighting P_{20} by this value we obtain

$$P_{20} = \frac{1}{2} \left[1 + \frac{\epsilon}{E(\epsilon, t_c)} \right] \tanh \left[\frac{E(\epsilon, t_c)}{2k_B T_e} \right]. \quad (5)$$

Combining this with parameters describing the charge sensor, which we assume exhibits a linear response, we arrive at Eq. (3) of the main text.

If we expand our model by including additional excited states or broadening mechanisms, P_{20} will still be $\sim 50\%$ at the (1,1)–(2,0) anticrossing, and Δ_{SB} can be accurately extracted as the distance between the midpoints of the singlet and triplet branches. On the other hand, extracted values of t_c (or T_e) can depend strongly on such changes. As a vivid example, we consider a process that dephases our system in the charge basis, possibly due to charge noise in ϵ or backaction from the measurement itself. We consider the density matrix describing our system, ρ , as it evolves under the coherent Hamiltonian H_S as well as Lindbladians describing thermalization and charge dephasing. Denoting the ground and excited eigenstates of H_S as $|-\rangle$ and $|+\rangle$ — not to be confused with the $|g\rangle_c$ and $|e\rangle_c$, the ground and excited states of a given charge configuration c — the master equation governing these dynamics is

$$\begin{aligned}
\dot{\rho}(t) &= -i[H_S, \rho(t)] + \mathcal{L}_{\text{thermal}}(\rho(t)) + \mathcal{L}_{\text{charge}}(\rho(t)), \\
\mathcal{L}_{\text{thermal}}(\rho) &= -\gamma \left(\langle + | \rho | + \rangle - \langle - | \rho | - \rangle - \tanh \left[\frac{E(\epsilon, t_c)}{2k_B T_e} \right] \right) (|+\rangle \langle +| - |-\rangle \langle -|) \\
&\quad - \frac{\gamma}{2} (\langle + | \rho | - \rangle |+\rangle \langle -| + \text{h.c.}), \\
\mathcal{L}_{\text{charge}}(\rho) &= -\frac{\kappa}{2} ({}_{11} \langle g | \rho | g \rangle_{20} |g\rangle_{11} {}_{20} \langle g| + \text{h.c.}),
\end{aligned} \tag{6}$$

where γ and κ are the thermalization and charge dephasing rates, respectively.

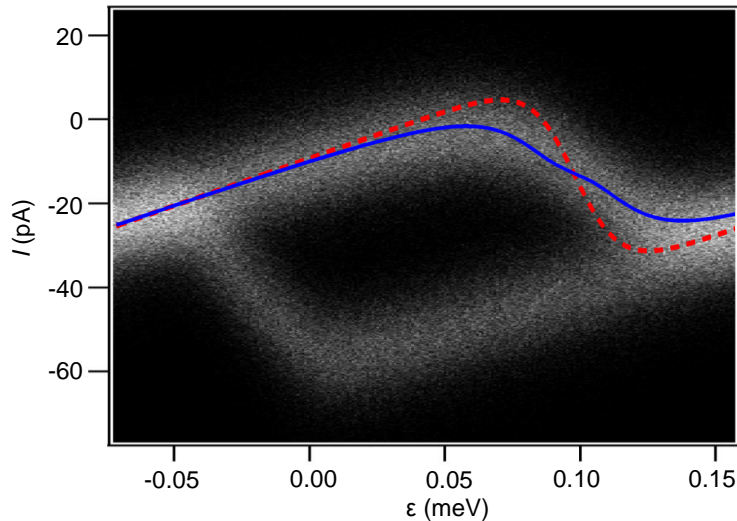


FIG. S3. Curve fits using t_c determined by spin funnel. With no charge dephasing (red dashed line), t_c is inadequate to match the observed broadening. With charge dephasing at $150\times$ the rate of thermalization (blue solid line), the broadening is recovered.

The quantity of interest in our measurement technique is the steady state probability $P_{20}^{\text{ss}} \equiv \lim_{t \rightarrow \infty} P_{20}(t) = \lim_{t \rightarrow \infty} {}_{20}\langle g | \rho(t) | g \rangle_{20}$. Numerically, we find that charge dephasing can lead to large, multiplicative broadening of P_{20}^{ss} as a function of ϵ . The degree of broadening depends on κ/γ , i.e. the ratio of charge- to thermal-decoherence rates. If charge dephasing is much faster than thermalization, this can increase the extracted t_c by two orders of magnitude or more. This may explain the large discrepancy in values of t_c extracted from fitting to Eqs. (1–3) of the main text (assuming fixed T_e) compared to other established techniques (see Supplemental Section VI); a κ of $\sim 150\gamma$ can resolve the discrepancy (see Fig. S3). However, including charge-state dephasing in the fit leaves T_e , t_c , κ , and γ as highly correlated parameters, and our fits are not sufficiently well-resolved to distinguish them. It is therefore too difficult to determine the impact of charge dephasing without an independent measurement of its magnitude, and so we mainly suggest it as an illustration of how broadening mechanisms can affect parameter estimation in our technique.

IV. RESOLVING SMALL Δ_{SB}

We now derive rough bounds on the minimum splitting that can be resolved with the technique outlined in the main text. Distinguishing the singlet and triplet branches is most difficult when they are similar in shape and close together, so we assume $t_c^{\text{S}} \approx t_c^{\text{T}}$ and $\Delta_{\text{SB}} < t_c$. In this limit, we can determine the vertical separation of the branches, η , by a linear expansion of the fit function. At $\epsilon - \epsilon^0 = \Delta_{\text{SB}}/2$, where separation between the branches is near its maximum,

$$\eta \approx \frac{I_{\text{amp}}}{2t_c} \tanh\left(\frac{t_c}{k_{\text{B}}T_e}\right) \Delta_{\text{SB}} \equiv \lambda \Delta_{\text{SB}}, \quad (7)$$

where we have introduced the slope λ to condense notation. If the singlet and triplet histograms have variance σ_I^2 and means separated by η , the combined histogram's total variance is given by

$$\sigma_{\text{tot}}^2 = \sigma_I^2 + P_{\text{S}}P_{\text{T}}\eta^2. \quad (8)$$

We can combine Eqs. (7) and (8) to solve for Δ_{SB} in terms of σ_{tot}^2 .

The precision of any estimate of σ_{tot}^2 is bounded by finite statistics. After N measurements, we can find an approximate $\tilde{\sigma}_{\text{tot}}^2$ which bounds the actual σ_{tot}^2 according to

$$\tilde{\sigma}_{\text{tot}}^2 = \sigma_{\text{tot}}^2 \left(1 \pm \frac{2\text{erf}^{-1}(C)}{\sqrt{N}} \right), \quad (9)$$

where erf^{-1} is the inverse error function and C is the confidence of the estimate. Writing versions of Eq. (8) for both actual and estimated variables and plugging the results into Eq. (9), we find a relation between the actual η and estimated $\tilde{\eta}$ which simplifies to

$$\tilde{\eta} = \eta \sqrt{1 \pm \frac{2\text{erf}^{-1}(C)}{\sqrt{N}} \left(1 + \frac{\sigma_I^2}{\eta^2 P_S P_T}\right)}. \quad (10)$$

The second error term implies N must scale with $(\sigma_I/\eta)^4$ to maintain a fixed uncertainty; this determines the minimum η that can be extracted with a reasonable number of measurements.

If the uncertainty in Eq. (10) is not overly large, we may wish to combine this with uncertainty in the other fit parameters to bound our overall confidence in Δ_{SB} . Let δX denote our fractional uncertainty in parameter X , i.e. $\tilde{X} = X(1 \pm \delta X)$. Eq. (9) can be understood as an expression of $\delta\sigma_{\text{tot}}$. Expanding Eqs. (7) and (8) to first order in each δ , and assuming that errors add quadratically, we find

$$\delta\Delta_{\text{SB}}^2 \lesssim \delta\eta^2 + \delta\lambda^2, \quad (11)$$

$$\delta\eta^2 \approx \left(\frac{\text{erf}^{-1}(C)}{\sqrt{N}} \left(1 + \frac{\sigma_I^2}{\eta^2 P_S P_T}\right)\right)^2 + \left(\frac{|P_S - P_T|}{2P_T} \delta P_S\right)^2 + \left(\frac{\sigma_I^2}{\eta^2 P_S P_T} \delta\sigma_I\right)^2. \quad (12)$$

$\delta\lambda$ can be expanded into a function of δt_c , δI_{amp} , and δT_e , but these are generally correlated fit parameters whose errors may not add independently, so we express their uncertainty collectively. If we assume that all fit parameters other than Δ_{SB} are known to high precision and keep only the shot noise term of Eq. (12), we recover Eq. (4) of the main text. Finally, it is worth emphasizing that all of the error sources discussed in this section are exclusive to small- Δ_{SB} fits. If Δ_{SB} is large enough to resolve the singlet and triplet branches, the fit is determined by horizontal distance rather than histogram width, and uncertainty is dominated by our measurement of the lever-arm, as described in Sec. I.

V. MEASURING Δ_{SB} OF THE INNER DOT

As mentioned in the main text, our excited-state spectroscopy technique can be performed at any charge boundary supporting spin blockade. Since the ‘inner’ dot $P2$ is more isolated from the bath, state preparation must be performed on an ‘outer’ dot (i.e. $P1$). Thus when measuring Δ_{SB}^{P2} , the same (1) spin preparation and (2) dephasing steps occur as when measuring Δ_{SB}^{P1} , followed by measurement near the region of SCC at the (1,1)-(0,2) charge

boundary, with the final charge reference measurement set within the (0,2) charge cell, as shown for (3) and (4) in Fig. S4a. These slight modifications of the pulse sequence allow Δ_{SB} to be measured on two quantum dots without changes to the electrostatic configuration.

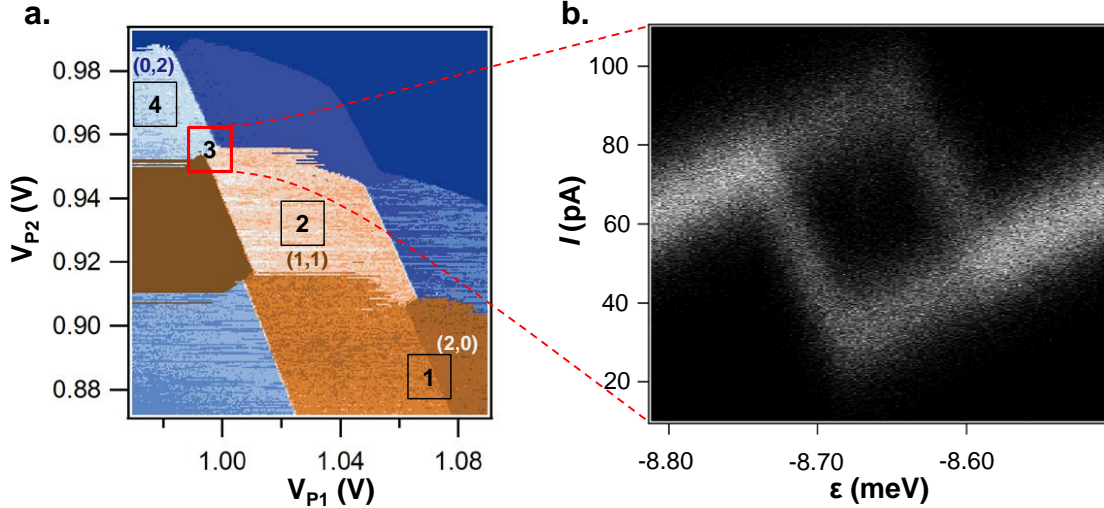


FIG. S4. **a**, Slight modifications in the pulse sequence are needed to extract Δ_{SB} of the inner dot ($P2$). The singlet initialization (1) and dephasing (2) steps remain the same, while measurement of spin blockade (3) is performed at the other charge-conserving boundary, (0,2)-(1,1), with the reference measurement point (4) set within the (0,2) charge cell. **b**, Although measurements of the inner dot share qualitative similarities with measurements of the outer $P1$ dot, the spin blockade region for $P2$ is at a negative detuning point ($\epsilon \approx -8.6$ meV).

VI. MEASUREMENT OF TUNNEL COUPLING

In addition to the two-electron ground-to-excited state splitting, Δ_{SB} , fitting data to Eq. (1) of the main text yields parameters describing the tunnel coupling, t_c . The solid markers of Figure S5 show t_c extracted from the data of Fig. 3 of the main text, fit assuming a fixed value of T_e . This is contrasted with t_c extracted from the more established spin funnel measurement technique, shown by open markers [7–9]. Notably, t_c extracted from spin-funnel measurements (which also consistently agree with Landau-Zener estimates of tunnel coupling, not shown here) are more than $10\times$ smaller than those estimated using the fit technique described in the main text. Even at the highest $X2$ voltages, where tunnel coupling dominates any temperature terms in the fit formula, the discrepancy persists. As

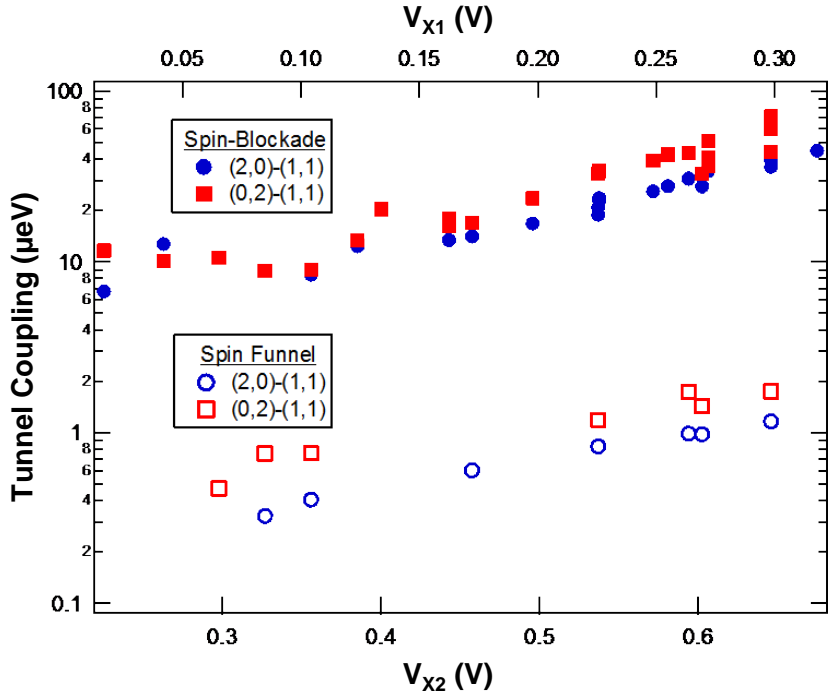


FIG. S5. Tunnel couplings extracted from spin-blockade fits compared to spin funnel measurements. Tunnel coupling at the $(2,0)$ - $(1,1)$ anticrossing (blue) and $(0,2)$ - $(1,1)$ anticrossing (red), extracted from a Fermi-Hubbard model fit to single-shot data using fit functions in main text at fixed T_e (solid markers) and tunnel couplings from spin funnel measurements (open markers).

noted in the main text, any effect that broadens the curves when fit to Eqs. (1–3) will lead to an overestimation of t_c , assuming that T_e has been reliably measured some other way. One such effect is the interplay of incoherent processes — charge state dephasing and eigenstate T_1 — during the measurement process, as discussed in Supplemental Section III. This suggests that this relatively simple, site-based coherent Fermi-Hubbard interaction model used to derive the fit functions in the main text is insufficient to describe real experimental data.

The ‘spin funnel’ measurements of the $(2,0)$ - $(1,1)$ and $(0,2)$ - $(1,1)$ tunnel couplings shown in Fig. S5 were performed by measuring the location of the $S_0 - T_{\pm}$ avoided crossing as a function of applied magnetic field. This established measurement technique offers a reliable comparison for the tunnel coupling extracted other ways. The sequence employed first prepares a singlet state, biases near the anticrossing of interest for a reference measurement, and then pulses to varying negative detunings (toward the $(1,1)$ cell center) with a dwell time of $10 \mu s$, after which the final pulse returns to the spin-to-charge readout window for

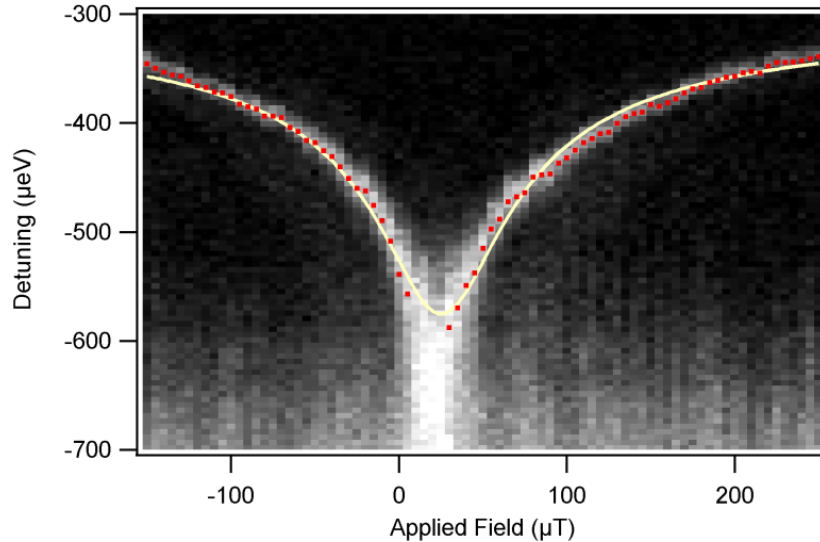


FIG. S6. Spin funnel measurement of tunnel coupling. Grayscale contrast highlights the probability of measuring a Pauli-blockaded spin state as a function of detuning and applied magnetic field. Red markers denote extracted peak position for each column. The yellow line shows a fit to the red markers using Eq. (13).

measurement. The $10 \mu\text{s}$ dwell time is chosen to be long enough to allow spin-orbit and hyperfine interactions to induce mixing between S_0 and T_{\pm} states at their anticrossing. This yields an increased probability of transitioning into the lower of the T_- and T_+ states at the detuning of that anticrossing (see Fig. S6).

The location of the $S_0 - T_{\pm}$ anticrossing is extracted by fitting a Gaussian profile to each column. The resulting peak location vs. magnetic field is then fit to the functional form:

$$\varepsilon = y_0 - \frac{t_c^2}{g\mu_B \sqrt{(B - B_0)^2 + B_{\perp}^2}}, \quad (13)$$

from which we extract the tunnel coupling, $t_c = 1.07 \pm 0.02 \mu\text{eV}$, as well as the vertical ($B_0 = 25 \mu\text{T}$) and horizontal ($B_{\perp} = 36 \mu\text{T}$) offset fields.

-
- [1] T. H. Stoof and Yu. V. Nazarov, “Time-dependent resonant tunneling via two discrete states,” *Phys. Rev. B* **53**, 1050–1053 (1996).
- [2] T. H. Oosterkamp, T. Fujisawa, W. G. van der Wiel, K. Ishibashi, R. V. Hijman, S. Tarucha,

- and L. P. Kouwenhoven, “Microwave spectroscopy of a quantum-dot molecule,” *Nature* **395**, 873–876 (1998).
- [3] I. T. Vink, T. Nooitgedagt, R. N. Schouten, L. M. K. Vandersypen, and W. Wegscheider, “Cryogenic amplifier for fast real-time detection of single-electron tunneling,” *Applied Physics Letters* **91**, 123512 (2007).
- [4] L. DiCarlo, H. J. Lynch, A. C. Johnson, L. I. Childress, K. Crockett, C. M. Marcus, M. P. Hanson, and A. C. Gossard, “Differential charge sensing and charge delocalization in a tunable double quantum dot,” *Phys. Rev. Lett.* **92**, 226801 (2004).
- [5] Dimitrie Culcer, Xuedong Hu, and S. Das Sarma, “Interface roughness, valley-orbit coupling, and valley manipulation in quantum dots,” *Phys. Rev. B* **82**, 205315 (2010).
- [6] M. L. V. Tagliaferri, P. L. Bavdaz, W. Huang, A. S. Dzurak, D. Culcer, and M. Veldhorst, “Impact of valley phase and splitting on readout of silicon spin qubits,” *Phys. Rev. B* **97**, 245412 (2018).
- [7] J. R. Petta, A. C. Johnson, J. M. Taylor, E. A. Laird, A. Yacoby, M. D. Lukin, C. M. Marcus, M. P. Hanson, and A. C. Gossard, “Coherent manipulation of coupled electron spins in semiconductor quantum dots,” *Science* **309**, 2180–2184 (2005), <http://science.sciencemag.org/content/309/5744/2180.full.pdf>.
- [8] J. R. Petta, J. M. Taylor, A. C. Johnson, A. Yacoby, M. D. Lukin, C. M. Marcus, M. P. Hanson, and A. C. Gossard, “Dynamic nuclear polarization with single electron spins,” *Phys. Rev. Lett.* **100**, 067601 (2008).
- [9] B. M. Maune, M. G. Borselli, B. Huang, T. D. Ladd, P. W. Deelman, K. S. Holabird, A. A. Kiselev, I. Alvarado-Rodriguez, R. S. Ross, A. E. Schmitz, M. Sokolich, C. A. Watson, M. F. Gyure, and A. T. Hunter, “Coherent singlet-triplet oscillations in a silicon-based double quantum dot,” *Nature* **481**, 344–347 (2012).